

NUMERICAL SIMULATION APPLIED TO CHARACTERIZE INDUCED ANISOTROPY IN DENSELY FRACTURED POROELASTIC MEDIA

Robiel Martínez Corredor^a and Juan E. Santos^b

^a*Facultad de Ingeniería, Universidad Nacional de La Plata, robielemartinez@yahoo.com*

^b*Instituto del Gas y del Petróleo, Facultad Ingeniería, Universidad de Buenos Aires, Department of Mathematics, Purdue University and Universidad Nacional de La Plata, jesantos48@gmail.com*

Keywords: finite elements, seismic anisotropy, boundary conditions, fractured Biot medium.

Abstract. Many hydrocarbon reservoirs are naturally fractured, and fracture orientation and distribution is an important subject of research, since fractures control the permeability of the reservoir. In this work presents a methodology to determine a viscoelastic transversely isotropic (VTI) medium long-wave equivalent to a fluid-saturated densely fractured poroelastic medium. The long-wave assumption implies that the VTI approximation is valid for fracture distances and fracture apertures much smaller than the average wavelengths of the predominant travelling waves. The fractures are modeled as discontinuities in displacements in the solid and fluid displacements and fluid pressures across fractures. The coefficients of the VTI medium are obtained using harmonic experiments on representative samples of the poroelastic material. In particular, the sensibility of VTI to variations in pore pressure is analyzed.

1 INTRODUCTION

Hydrocarbon reservoir rocks have in many cases plane compliant discontinuities, like fractures and faults, that in general control the hydrocarbon flow and production in the reservoir [Gurevich, B. \(2003\)](#), [Gurevich, B. et al. \(2009\)](#). Also, in many cases reservoirs rocks contain dense sets of fractures aligned in preferred directions. A fracture in a fluid-saturated poroelastic - Biot - medium is a very thin compliant and highly permeable layer, with the layer thickness on the order of millimeters. In this paper, fractures are modeled using the boundary conditions in [Nakawa, S. and Schoenberg, M. A. \(2007\)](#). These boundary conditions impose continuity of the total stress components, pressure discontinuities proportional to average fluid velocities across the fracture, and displacement discontinuities proportional to stress components and average fluid pressures along the fracture. Wave-induced fluid flow [Santos, J. E. et al. \(2011\)](#); [Santos et al. \(2014\)](#), by which the fast waves are converted to slow (diffusive) Biot waves when traveling across fractures (mesoscopic-loss) is well represented by these conditions.

A Biot medium with a dense set of horizontal fractures behaves as a TIV medium for average fracture distances much smaller than the predominant wavelengths of the travelling waves.

The relaxed and unrelaxed stiffnesses of the equivalent poro-viscoelastic medium to a finely layered horizontally homogeneous material were determined in [Gelinsky, S. and Shapiro, S. A. \(1997\)](#). Later, the five complex and frequency-dependent stiffnesses of the equivalent TIV medium were derived in [Krzikalla, F. and Müller, T. \(2011\)](#).

This work uses the set of five harmonic FE compressibility and shear experiments described in [Santos, J. E. et al. \(2011\)](#); [Santos et al. \(2014\)](#) to determine a long-wave equivalent TIV medium to a highly heterogeneous horizontally fractured Biot medium.

The FE results are first validated comparing the results using the boundary conditions to model fractures with those obtained with harmonic FE experiments with fractures represented as thin layers as in [Santos et al. \(2014\)](#). Then the procedure is applied to analyze the response of a fractured Biot media varying the volume fraction of the heterogeneities, represented as stochastic fractals.

A FRACTURED BIOT MEDIUM AND THE EQUIVALENT TIV MEDIUM

We consider a fractured isotropic Biot medium $\Omega = (0, L_1) \times (0, L_3)$ with boundary Γ in the (x_1, x_3) -plane, with x_1 and x_3 being the horizontal and vertical coordinates, respectively. Let \mathbf{u}_s and $\tilde{\mathbf{u}}_f$, denote the averaged displacement vectors of the solid and fluid phases, respectively. Let $\mathbf{u}_f = \phi(\tilde{\mathbf{u}}_f - \mathbf{u}_s)$ be the relative fluid displacement, where ϕ denotes the porosity and set $\mathbf{u} = (\mathbf{u}_s, \mathbf{u}_f)$. Let $\varepsilon(\mathbf{u}_s)$, $\boldsymbol{\tau}(\mathbf{u})$ and $p_f(\mathbf{u})$ denote the strain tensor of the solid, the stress tensor of the bulk material and the fluid pressure, respectively. The stress-strain relations are ([Biot, M.A., 1962](#)):

$$\boldsymbol{\tau}_{st}(\mathbf{u}) = 2G \varepsilon_{st}(\mathbf{u}_s) + \delta_{st}(\lambda_U \nabla \cdot \mathbf{u}_s + \alpha M \nabla \cdot \mathbf{u}_f), \quad (1)$$

$$p_f(\mathbf{u}) = -\alpha M \nabla \cdot \mathbf{u}_s - M \nabla \cdot \mathbf{u}_f. \quad (2)$$

The coefficient G is the shear modulus of the dry matrix, while the other coefficients in (1)-(2) can be determined in terms of K_s , K_m and K_f , the bulk moduli of the solid grains, dry matrix and saturant fluid, respectively, ([Carcione, 2007](#)). Biot's equations in the diffusive range and in the absence of external forces are ([Biot, M.A., 1962](#)):

$$\nabla \cdot \boldsymbol{\tau}(\mathbf{u}) = 0, \quad (3)$$

$$i\omega \mathbf{u}_f + \frac{\mu}{\kappa} \nabla p_f(\mathbf{u}) = 0, \quad (4)$$

where $i = \sqrt{-1}$, ω is the angular frequency, μ is the fluid viscosity and κ is the frame permeability.

Assume that Ω has a set of $J^{(f)}$ horizontal fractures $\Gamma^{(f,l)}$, $l = 1, \dots, J^{(f)}$, each one of length L_1 and aperture h , so that $\Omega = \cup_{l=1}^{J^{(f)}+1} R^{(l)}$. Consider a fracture $\Gamma^{(f,l)}$ and the two rectangles $R^{(l)}$ and $R^{(l+1)}$ having as a common side $\Gamma^{(f,l)}$. Let $\nu_{l,l+1}$ and $\chi_{l,l+1}$ be the unit outer normal and a unit tangent (oriented counterclockwise) on $\Gamma^{(f,l)}$ from $R^{(l)}$ to $R^{(l+1)}$. Let $[\mathbf{u}_s]$, $[\mathbf{u}_f]$ denote the jumps of the solid and fluid displacement vectors at $\Gamma^{(f,l)}$, i.e. $[\mathbf{u}_s] = \left(\mathbf{u}_s^{(l+1)} - \mathbf{u}_s^{(l)} \right) |_{\Gamma^{(f,l)}}$, where $\mathbf{u}_s^{(l)}$ denotes the displacement values in $R^{(l)}$. The following boundary conditions at $\Gamma^{(f,l)}$ are derived in Nakawa, S. and Schoenberg, M. A. (2007):

$$[\mathbf{u}_s \cdot \nu_{l,l+1}] = \eta_N \left((1 - \alpha \tilde{B}(1 - \Pi)) \boldsymbol{\tau}(\mathbf{u}) \nu_{l,l+1} \cdot \nu_{l,l+1} - \alpha \frac{1}{2} \left((-p_f^{(l+1)}) + (-p_f^{(l)}) \right) \Pi \right), \tag{5}$$

$$[\mathbf{u}_s \cdot \chi_{l,l+1}] = \eta_T \boldsymbol{\tau}(\mathbf{u}) \nu_{l,l+1} \cdot \chi_{l,l+1}, \tag{6}$$

$$[\mathbf{u}_f \cdot \nu_{l,l+1}] = \alpha \eta_N \left(-\boldsymbol{\tau}(\mathbf{u}) \nu_{l,l+1} \cdot \nu_{l,l+1} + \frac{1}{\tilde{B}} \frac{1}{2} \left((-p_f^{(l+1)}) + (-p_f^{(l)}) \right) \right) \Pi, \tag{7}$$

$$(-p_f^{(l+1)}) - (-p_f^{(l)}) = \frac{i\omega\mu\Pi}{\hat{\kappa}} \frac{1}{2} \left(\mathbf{u}_f^{(l+1)} + \mathbf{u}_f^{(l)} \right) \cdot \nu_{l,l+1}. \tag{8}$$

$$\boldsymbol{\tau}(\mathbf{u}) \nu_{l,l+1} \cdot \nu_{l,l+1} = \boldsymbol{\tau}(\mathbf{u}) \nu_{l+1,l} \cdot \nu_{l+1,l} \tag{9}$$

$$\boldsymbol{\tau}(\mathbf{u}) \nu_{l,l+1} \cdot \chi_{l,l+1} = \boldsymbol{\tau}(\mathbf{u}) \nu_{l+1,l} \cdot \chi_{l+1,l}. \tag{10}$$

Here η_N and η_T are the normal and tangential fracture compliances, respectively and $\hat{\kappa} = \kappa/h$, with h denoting the fracture aperture. The fracture dry plane wave modulus $H_m = K_m + (4/3)G$ and the dry fracture shear modulus G are defined in terms of the fracture aperture and the fracture compliances as

$$\eta_N = \frac{h}{H_m}, \quad \eta_T = \frac{h}{G}.$$

Besides, $\Pi(\epsilon) = \tanh \epsilon/\epsilon$, $\tilde{B} = (\alpha M)/H_U$ (H_U is the undrained plane wave modulus) and

$$\epsilon = \frac{(1+i)}{2} \left(\frac{\omega\mu\alpha\eta_N}{2\tilde{B}\hat{\kappa}} \right)^{1/2}, \quad \alpha = 1 - K_m/K_s.$$

Here $H_U = K_U + \frac{4}{3}G$ is the undrained plane wave modulus, where

$$K_U = K_s \frac{K_m + \Xi}{K_s + \Xi}, \quad \Xi = \frac{K_f(K_s - K_m)}{\phi(K_s - K_f)}. \tag{11}$$

A horizontally fractured Biot medium behaves as a TIV medium with vertical symmetry axis at long wavelengths. As in Gelinsky, S. and Shapiro, S. A. (1997); Krzikalla, F. and Müller, T.

(2011); Carcione (2007), the stress-strain relations of the equivalent TIV medium are:

$$\sigma_{11}(\tilde{\mathbf{u}}_s) = p_{11} \epsilon_{11}(\tilde{\mathbf{u}}_s) + p_{12} \epsilon_{22}(\tilde{\mathbf{u}}_s) + p_{13} \epsilon_{33}(\tilde{\mathbf{u}}_s), \quad (12)$$

$$\sigma_{22}(\tilde{\mathbf{u}}_s) = p_{12} \epsilon_{11}(\tilde{\mathbf{u}}_s) + p_{11} \epsilon_{22}(\tilde{\mathbf{u}}_s) + p_{13} \epsilon_{33}(\tilde{\mathbf{u}}_s), \quad (13)$$

$$\sigma_{33}(\tilde{\mathbf{u}}_s) = p_{13} \epsilon_{11}(\tilde{\mathbf{u}}_s) + p_{13} \epsilon_{22}(\tilde{\mathbf{u}}_s) + p_{33} \epsilon_{33}(\tilde{\mathbf{u}}_s), \quad (14)$$

$$\sigma_{23}(\tilde{\mathbf{u}}_s) = 2 p_{55} \epsilon_{23}(\tilde{\mathbf{u}}_s), \quad (15)$$

$$\sigma_{13}(\tilde{\mathbf{u}}_s) = 2 p_{55} \epsilon_{13}(\tilde{\mathbf{u}}_s), \quad (16)$$

$$\sigma_{12}(\tilde{\mathbf{u}}_s) = 2 p_{66} \epsilon_{12}(\tilde{\mathbf{u}}_s). \quad (17)$$

Here $\tilde{\mathbf{u}}_s$, $\sigma(\tilde{\mathbf{u}}_s)$ and $\epsilon(\tilde{\mathbf{u}}_s)$ are the displacement, the stress and the strain tensor at the macroscale, respectively.

To determine the coefficients in (12)-(17), we applied five compressibility and shear tests on representative 2D samples of fractured poroelastic material. Each test is associated with a boundary value problem for Biot's equations (3) with the fracture boundary conditions (5)-(10) and additional boundary conditions representing those compressibility and shear tests. These boundary value problems were solved using the FE method. Figure 1 illustrates the five tests used to determine the stiffness coefficients. A detailed description of the procedure can be found in (Carcione, J. M. et al., 2011) and (Santos, J. E. et al., 2011).

In order to relate the pore and confining pressure to the fracture compliances, following Brajanovski et al. (2005), Daley et al. (2006) and Carcione et al. (2012), let us define the compliances

$$Z_N = \eta_N/L, \quad Z_T = \eta_T/L$$

characterizing the fractures, where L is the fracture distance.

The compliances Z_N and Z_T are assumed to be dependent on the effective stress $\sigma = p_c - p$, where p_c is the confining pressure and p the pore pressure as

$$Z_q = Z_{q\infty} + (Z_{q0} - Z_{q\infty}) e^{(-\sigma/\tau_q)} \quad q = N, T \quad (18)$$

where Z_{q0} , $Z_{q\infty}$ y τ_q are constants.

2 NUMERICAL EXAMPLES

The FE procedure was used to determine the complex stiffnesses $p_{IJ}(\omega)$; the associated energy velocities and dissipation coefficients were computed using the formulas given in Carcione (2007).

First we validate the results obtained modeling the fractures using (5)-(10) and comparing them with those obtained for fractures modeled as thin layers. The sample is a square of side length 5mm, with 4 equally spaced fractures of aperture $h = 5\text{mm}$. The FE meshes were a 100×109 uniform mesh for fractures as fine layers and a 100×100 uniform mesh for fractures modeled using the boundary conditions (5)-(10). The saturant fluid is water with density 1000 Kg/m^3 , bulk modulus 2.25 GPa and viscosity $0.001 \text{ Pa}\cdot\text{s}$. Frequency is 35Hz.

The sample contains Material 1 in the background and Material 2 in the fractures, taken from Nakawa, S. and Schoenberg, M. A. (2007). Also contains a 10% volume fraction of Material 3 (the heterogeneities) with its material properties being averages of the other 2 materials and having a fractal spatial distribution over both background and fractures (See Figure 2).

Figures 3-4 exhibit a very good fit with the fine layer model for fractures. Strong velocity and Q anisotropy is observed. Here 0 degrees and 90 degrees correspond to waves arriving

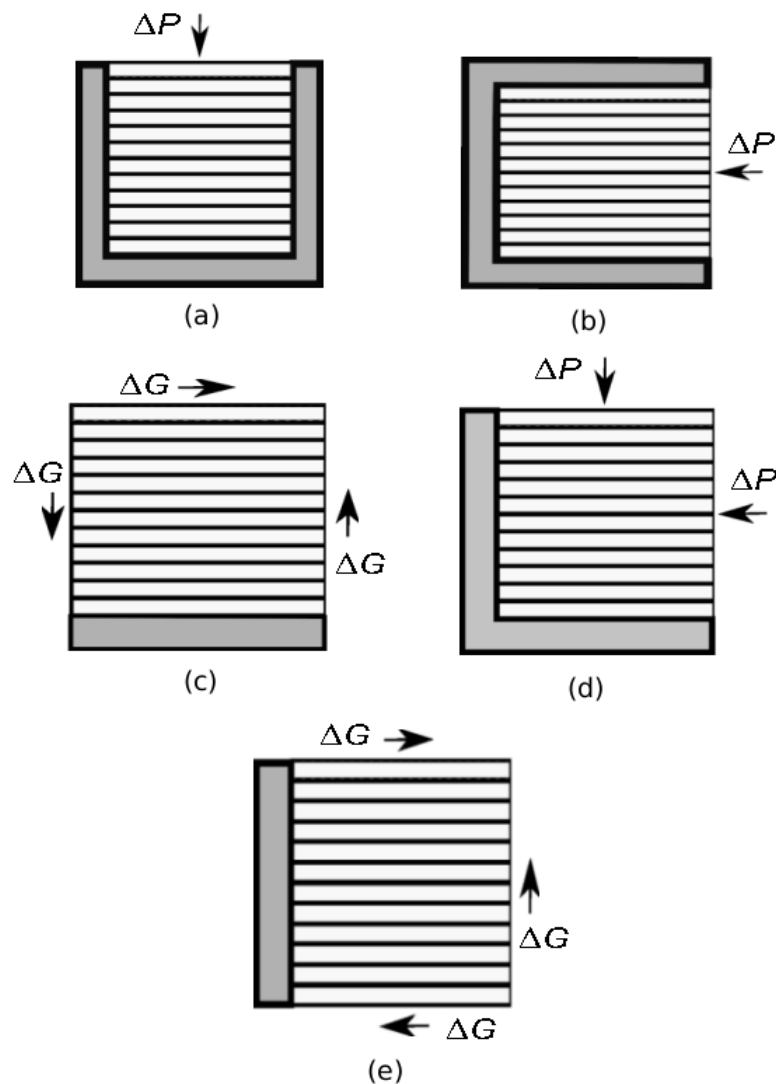


Figure 1: Figures 1(a)-1(e) illustrate the five experiments needed to compute the stiffnesses components. Figures 1(a) and 1(b) show how to compute p_{33} and p_{11} , respectively. Also, performing the experiments shown in 1(c) and 1(e) determine the stiffnesses p_{55} and p_{66} . Figure 1(d) displays the experiment to determine p_{13} .

parallel and normal to the fracture layering, respectively. Figure 3-(a) shows that attenuation for qP waves is higher for angles between 60 and 90 degrees, while in Figure 3-(b) is seen that for qSV the higher attenuation occurs for angles between 60 and 90 degrees. Also, in Figure 4 is seen that qSV waves have stronger velocity anisotropy than qP waves, with qSV waves having the typical cuspidal triangles (or triplications), observed previously in fractured media (Carcione (1996)).

In the second experiment fractures are modeled using the boundary conditions (5)-(10) to analyze the sensitivity of velocities and attenuation to variations in the volume fractions of Material 3 in the sample. The sample is square with side length 1cm with 9 equally spaced fractures of aperture $h = 1\text{mm}$. We used a 100×100 uniform mesh. Figure 5 displays the fractal sample for the case of 10% volume fraction of Material 3.

Figure 6-(a) shows that qP attenuation is higher for angles between 60 and 90 degrees and almost independent of the volume fraction of Material 3 present in the sample. Instead from Figure 6-(b) it is concluded that qSV attenuation changes significantly for different proportions

Rock properties			
	Material 1	Material 2	Material 3
K_s (GPa)	36	36	36
ρ_s (Kg/m ³)	2700	2700	2700
ϕ	0.15	0.5	0.65
K_m (GPa)	9.0	0.0055	0.0044
G (GPa)	7.0	0.0033	0.0022
κ (D)	0.1	10.0	20.0

Table 1: Physical properties of the solid materials used in the numerical examples.

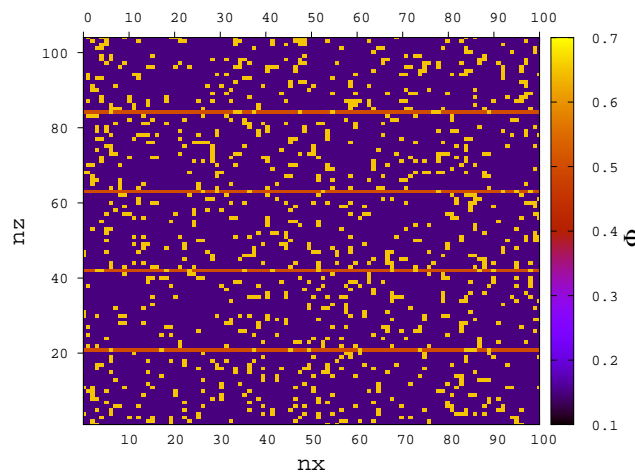


Figure 2: Porosity distribution for 10% volume fraction of Material 3, which is fractally distributed in both background and fractures, modeled as thin layers.

of material 3 in the sample.

Figures 7-(a) and 7-(b) shows that both qP and qSV energy velocity values decrease as the volume fraction of Material 3 increases, mainly due to the high porosity of this material. Besides, note that the fractal nature of the spatial distribution of Material 3 breaks the symmetry of the curves of qSV energy velocities (see the cuspidal triangles).

Finally, to analyze the pore pressure effect on velocities and attenuation, we choose a square sample of side length 10 m, with a fracture distance equal to 1 m ($L = 1$ m). The background is homogeneous and isotropic, with the properties of Material 1. Fractures are also homogeneous and isotropic with $K_s = 36$ GPa, $\rho_s = 2700$ Kg/m³, $\phi = 0.5$ y $\kappa = 10$ D. The fracture thickness is $h = 1$ mm. The compliances vary as in Daley et al. (2006) as follows:

$$G_b Z_{N_0} = 1.5, \quad (\lambda_{U,b} + 2G_b) Z_{T_0} = 0.25 \quad (19)$$

where G_b is the background shear modulus and

$$\lambda_{U,b} = K_{U,b} - \frac{2}{3}G_b \quad (20)$$

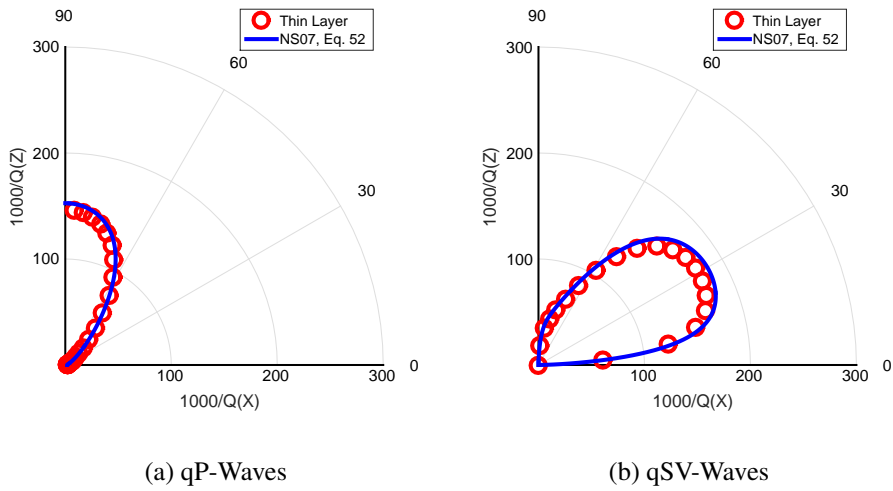


Figure 3: Dissipation factor at 35Hz. The solid line indicate the numerical values.

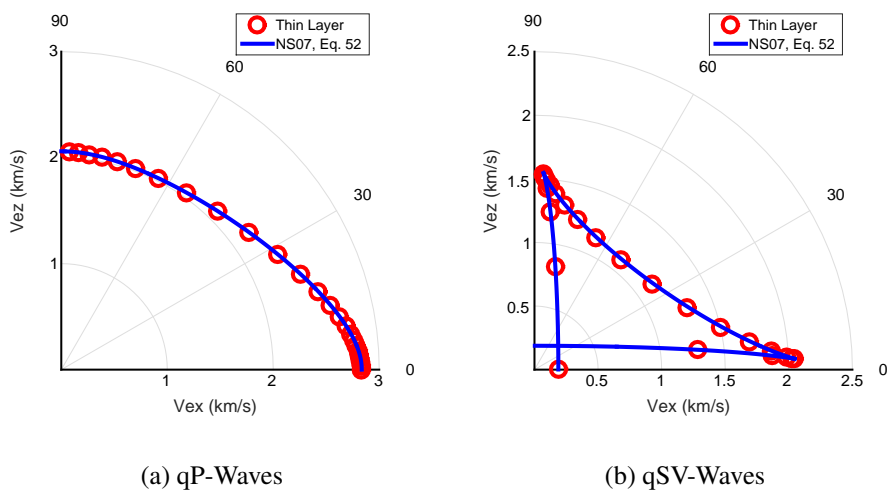


Figure 4: Polar representation of the energy velocity vector at 35Hz. The solid line indicate the numerical values.

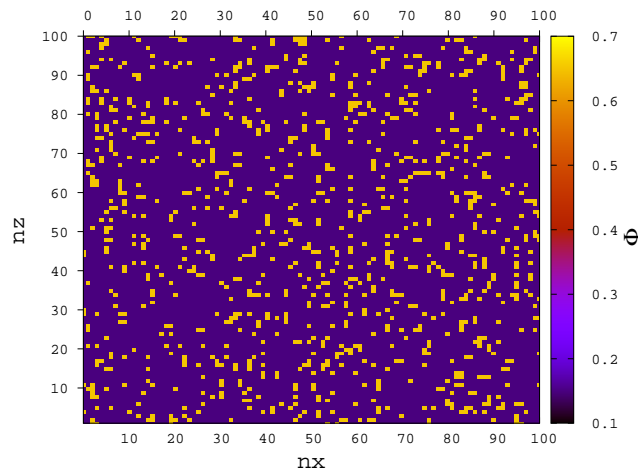


Figure 5: Porosity distribution for 10% volume fraction of Material 3, which is fractally distributed in both background and fractures. Fractures are represented using the boundary conditions (5)-(10).

and $K_{U,b}$ in (20) is the undrained bulk modulus defined in (11). Also,

$$Z_{T_\infty} = Z_{T_0}/5, Z_{N_\infty} = Z_{N_0}/2, \tau_T = 2MPa, \text{ and } \tau_N = 2MPa.$$

As shown in Carcione et al. (2012), let us consider a constant confining pressure $p_c = 30$ MPa and two pore pressures 5 and 28 MPa, normal and overpressure values, respectively. Figure 8 shows that attenuation anisotropy is stronger in the case of overpressure. Also, velocity anisotropy becomes stronger with increasing pore pressure, as seen in Figure 9.

3 CONCLUSIONS

This work used a finite element procedure to determine the five complex and frequency-dependent stiffnesses of the TIV medium equivalent to a horizontally highly heterogeneous fractured Biot medium, with fractures represented as boundary conditions. The procedure was validated comparing the results with those obtained for fractures modeled as fine layers and then applied to analyze the sensitivity of velocities and attenuation to variations in the proportions of heterogeneities present in the sample. In all cases, the experiments show that fractures induce strong velocity and attenuation anisotropy. Also, it was observed that qSV attenuation is very sensitive to changes in proportions of the heterogeneities, while qP attenuation is almost independent of these proportions. Also, energy velocities decrease as the volume fraction of the heterogeneities increase, and the fractal nature of the heterogeneities breaks the symmetry of the curves of qSV energy velocities. Finally it is concluded that an increase in pore pressure causes increases in velocity and attenuation anisotropy.

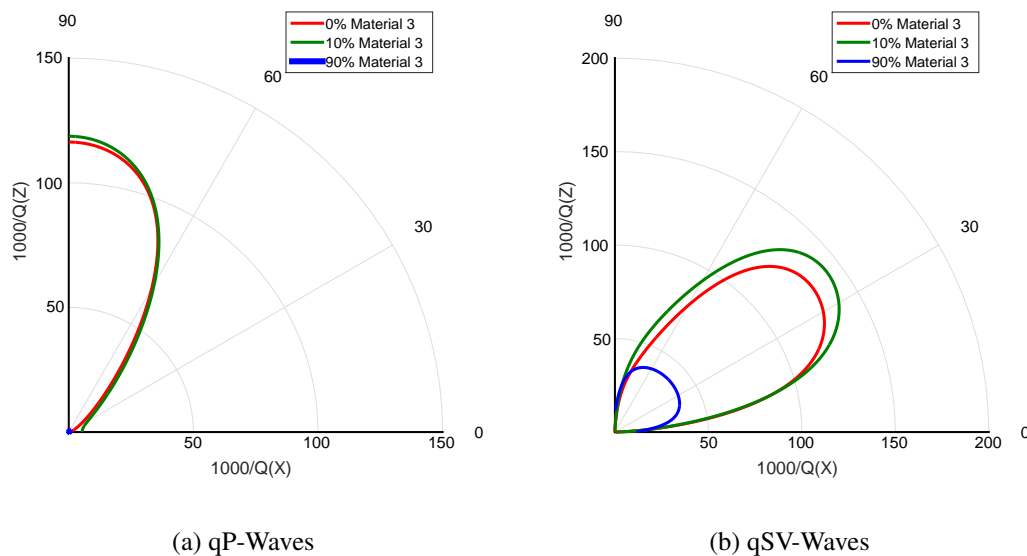


Figure 6: Dissipation factor at 35Hz for different volume fractions of Material 3. Fractures are represented using the boundary conditions (5)-(10).

REFERENCES

- Biot, M.A. Mechanics of deformation and acoustic propagation in porous media. *Journal of Applied Physics*, 33:1482–1498, 1962.
- Brajanovski M., Gurevich B., and Schoenberg M. A model for p-wave attenuation and dispersion in a porous medium permeated by aligned fractures. *Geophysical Journal International*, 163(1):372–384, 2005. ISSN 1365-246X. doi:10.1111/j.1365-246X.2005.02722.x.
- Carcione J.M. Plane-layered models for the analysis of wave propagation in reservoir environments1. *Geophysical Prospecting*, 44(1):3–26, 1996. ISSN 1365-2478. doi:10.1111/j.1365-2478.1996.tb00136.x.
- Carcione J.M. *Wave fields in real media: Wave Propagation in Anisotropic, Anelastic, Porous and Electromagnetic Media, Handbook of Geophysical Exploration, vol. 38*. Elsevier (2nd edition, revised and extended), 2007.
- Carcione J.M., Picotti S., and Santos J.E. Numerical experiments of fracture-induced velocity and attenuation anisotropy. *Geophysical Journal International*, 191(3):1179–1191, 2012. ISSN 1365-246X. doi:10.1111/j.1365-246X.2012.05697.x.
- Carcione, J. M., Santos, J. E., and Picotti, S. Anisotropic poroelasticity and wave-induced fluid flow. Harmonic finite-element simulations. *Geophysics Journal International*, 186:1245–1254, 2011.
- Daley T.M., Schoenberg M.A., Rutqvist J., and Nihei K.T. Fractured reservoirs: An analysis of coupled elastodynamic and permeability changes from pore-pressure variation. *GEOPHYSICS*, 71(5):O33–O41, 2006. doi:10.1190/1.2231108.
- Gelinsky, S. and Shapiro, S. A. Poroelastic Backus-averaging for anisotropic, layered fluid and gas saturated sediments. *Geophysics*, 62:1867–1878, 1997.
- Gurevich, B. Elastic properties of saturated porous rocks with aligned fractures. *Journal of Applied Geophysics*, 54:203–218, 2003.
- Gurevich, B., Brajanovski, M., Galvin, R. J., Müller, T. M., and Toms-Stewart, J. P-wave

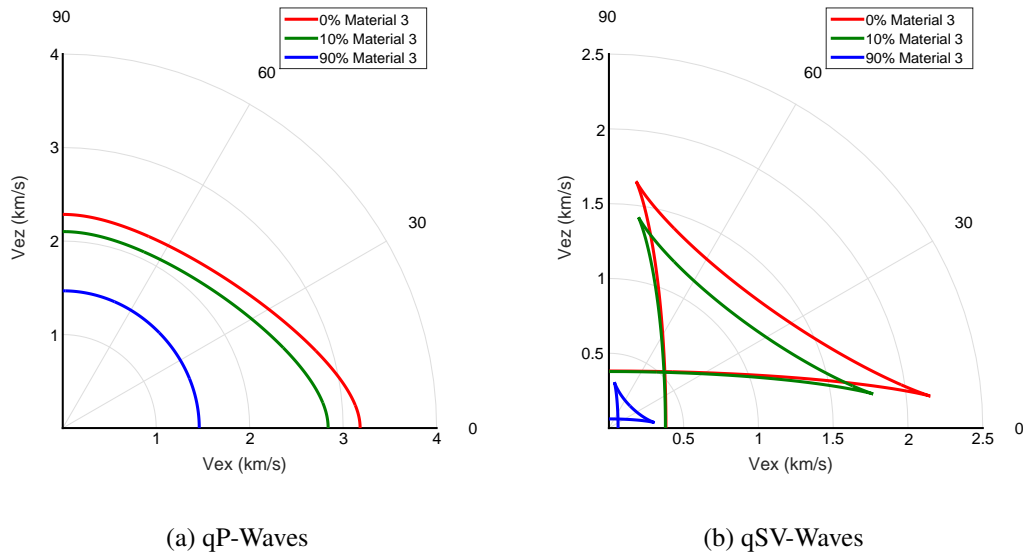


Figure 7: Polar representation of the energy velocity vector at 35Hz for different volume fractions of Material 3. Fractures are represented using the boundary conditions (5)-(10).

dispersion and attenuation in fractured and porous reservoirs—poroelasticity approach. *Geophysical Prospecting*, 57:225–237, 2009.

Krzikalla, F. and Müller, T. Anisotropic P-SV-wave dispersion and attenuation due to interlayer flow in thinly layered porous rocks. *Geophysics*, 76:WA135, 2011.

Nakawa, S. and Schoenberg, M. A. Poroelastic modeling of seismic boundary conditions across a fracture. *Journal of the Acoustical Society of America*, 122:831–847, 2007.

Santos J.E., Corredor R.M., and Carcione J.M. Seismic velocity and q anisotropy in fractured poroelastic media. *International Journal of Rock Mechanics and Mining Sciences*, 70(Complete):212–218, 2014. doi:10.1016/j.ijrmms.2014.05.004.

Santos, J. E., Carcione, J. M., and Picotti, S. Analysis of mesoscopic loss effects in anisotropic poroelastic media using harmonic finite element simulations. *81th Annual International Meeting, SEG, Expanded Abstracts*, pages 2211–2215, 2011.

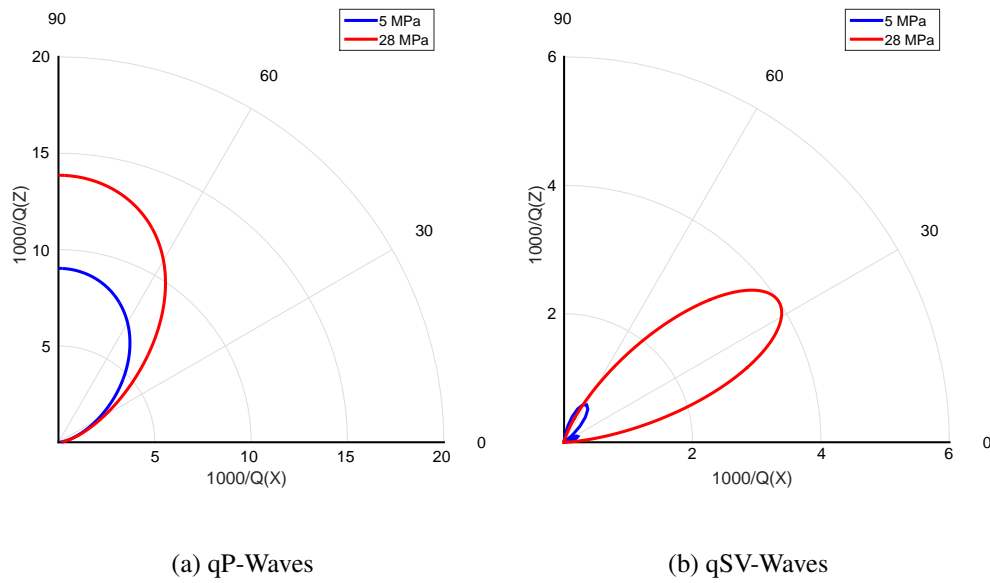
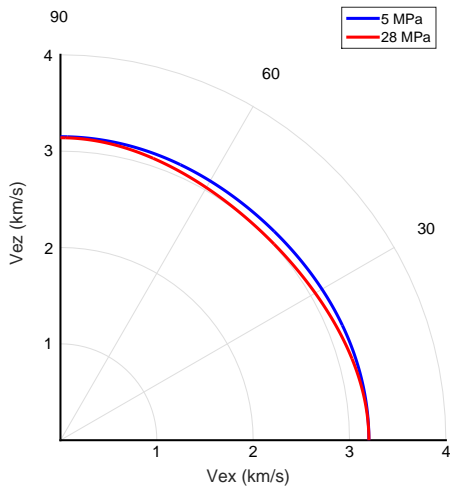
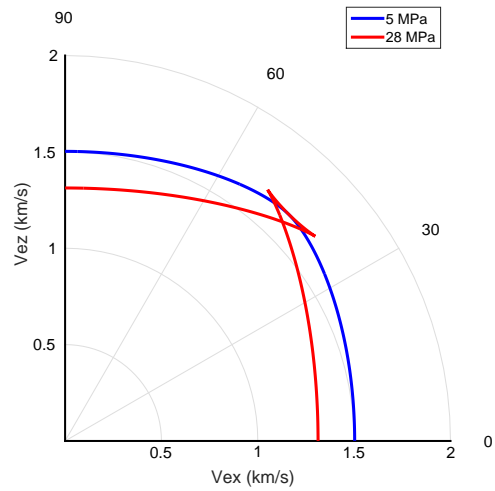


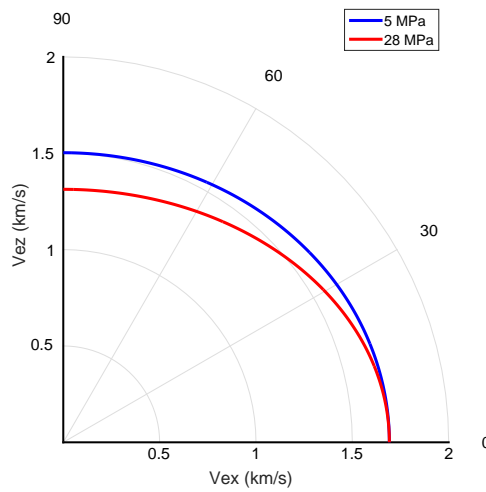
Figure 8: Dissipation factor at 60Hz for fractures with normal pore pressure (blue line, 5 MPa) and overpressure (red line, 28 MPa). Fractures are represented using the boundary conditions (5)-(10).



(a) qP-Waves



(b) qSV-Waves



(c) SH-Waves

Figure 9: Polar representation of the energy velocity vector at 60Hz for fractures with normal pore pressure (blue line, 5 MPa) and overpressure (red line, 28 MPa). Fractures are represented using the boundary conditions (5)-(10).